Composites: Part A 165 (2023) 107346

Contents lists available at ScienceDirect

Composites Part A

journal homepage: www.elsevier.com/locate/compositesa

Extraction of mix-mode cohesive laws of a unidirectional composite undergoing delamination with large-scale fibre bridging

R. Erives [a,*], B.F. Sørensen [a], S. Goutianos [b]

[a] Technical University of Denmark, DTU Wind and Energy Systems, Risø Campus, DK-4000, Roskilde, Denmark
[b] Norwegian University of Science and Technology, Department of Manufacturing and Civil Engineering, 2815 Gjøvik, Norway

ARTICLE INFO

Keywords:
Mixed-mode cohesive laws
Mixed-mode delamination
Fibre bridging
Potential based cohesive laws
R-curves

ABSTRACT

A novel method is proposed for extracting the mixed-mode cohesive laws of composite materials undergoing delamination with large-scale fibre bridging. In the approach, the mixed-mode cohesive laws are derived from a potential function expressed in cylindrical coordinates with the magnitude and phase angle between the normal and tangential end-openings. The potential function is mapped using experimental R-curves in terms of the J-integral and the end-openings. The mixed-mode cohesive laws describe both the crack tip (high tractions, small separations) and bridging region (small tractions, high separations). The extracted mixed-mode cohesive tractions are fully coupled, i.e., both the normal and shear traction depend on the normal and tangential openings. The peak normal and shear tractions were found to be at a mixed mode opening.

1. Introduction

For most composite structures such as wind turbine rotor blades, delamination has been identified as one of the most concerning damage mechanisms due to its effect on both the overall stiffness and load-carrying capacity of the structure [1]. Currently, there are many cohesive zone models (CZM) that can simulate mixed-mode delamination both under monotonic [2–7], and cyclic loading [8–13]. However, virtually all of these models rely on idealised (simplified), uncoupled (or coupled in a predefined manner e.g. bi-linear [2,3,6,13], trapezoidal [6], and exponential [14,15]) cohesive laws. The shape of idealised cohesive laws is typically defined a priori instead of being derived or measured. The use of idealised cohesive laws is based on the assumption that the shape of the cohesive law is not critical as long as the fracture energy is correct. While this holds true for small-scale fracture (i.e. when the fracture process zone is contained in the K-dominated region) [16], it is not correct under large-scale fracture [17]. As such, having a predefined shape of the cohesive laws presents limitations for analyses of large-scale fracture process zone problems. The correct shape of the cohesive law is needed to compute the crack growth stability (transition from stable to unstable crack growth) of a composite structure [18]. In general, the shape of the cohesive law conveys much information about the fracture behaviour of a material as pointed out by Sørensen and Kirkegaard [19].

The predictive ability and accuracy of cohesive zone models (CZM) largely depend on the accurate determination of the cohesive parameters defining the traction–separation law [20]. It follows that the experimental determination of cohesive laws is crucial to the accuracy of CZM. Historically, the fracture mechanics characterisation of materials has mainly been built around linear elastic fracture mechanics (LEFM), i.e. measuring the critical value of the energy release rate associated with onset at crack growth [21–26], not to measure cohesive laws. However, now with cohesive laws as the relevant material laws to determine, it is preferable to use test specimens for which a J-integral equation exists, since the path-independence property of the J-integral provides a connection between the cohesive law and the applied load [27]. A prominent class of specimens are double cantilever beams (DCB) loaded with bending moments [28]. For these specimens, J-integral equations are independent of the size of the FPZ and details of the cohesive laws. Furthermore, these specimens ensure stable crack growth such that the entire fracture resistance, from the onset of crack growth to steady-state (fully developed bridging zone) can be measured. Assuming that the cohesive laws are derived from a potential function, mixed-mode cohesive laws can be obtained by partial differentiation, since the J-integral value equals the potential function [19]. In an earlier study, the potential function was expressed in terms of a sum of products of Chebyshev polynomials, and mixed-mode bridging laws were determined for a laminate undergoing large-scale fibre bridging [29]. A drawback of the approach is that the cohesive tractions would "wobble" in areas where there are no experimental data. Therefore, this approach requires large series of mixed-mode experiments to cover the entire region of end-openings [19,29].

* Corresponding author.
E-mail address: riea@dtu.dk (R. Erives).

https://doi.org/10.1016/j.compositesa.2022.107346
Received 26 September 2022; Received in revised form 16 November 2022; Accepted 24 November 2022
Available online 26 November 2022

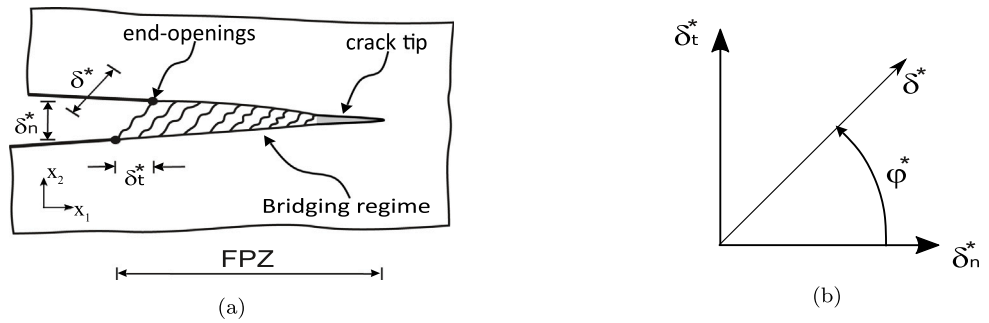

Fig. 1. Schematic of a crack under mixed-mode loading and exhibiting large-scale bridging (a) Definition of normal, tangential, and combined end-openings [30], (b) Cylindrical coordinate system used for the end-openings.

The present study aims to develop a systematic procedure to characterise the mixed-mode delamination of UD composites exhibiting large-scale bridging in terms of their mixed-mode cohesive laws. This is done by defining a potential function that depends on parameters extracted from experimental R-curves (using the J-integral). This function closely matches the experimentally measured mixed-mode fracture resistance and is used to determine the mixed-mode cohesive laws of a UD composite undergoing large-scale bridging. The proposed procedure is divided into four parts, namely the experimental determination of the R-curves, the extraction of fracture parameters for each mixed-mode, the determination of a potential function that covers the fracture resistance of all mixed-modes, and the derivation of the cohesive tractions.

2. Theory: Cylindrical mixed-mode cohesive law

The theoretical framework of the proposed method is described in detail elsewhere [30]. However, the most important concepts are presented here for the sake of completeness.

It is assumed that the mixed-mode cohesive laws of a material can be derived from a potential function [14,31,32], Φ, (to be determined) so that

$$\sigma_n = \frac{\partial \Phi}{\partial \delta_n}, \text{ and } \sigma_t = \frac{\partial \Phi}{\partial \delta_t}, \tag{1}$$

where σ_n and σ_t are the normal and the shear traction respectively, and δ_n and δ_t are the normal and tangential openings. Then, the J-integral evaluated locally around the cohesive zone gives [19]

$$J(\delta_n^*, \delta_t^*) = \Phi(\delta_n^*, \delta_t^*). \tag{2}$$

Here, an asterisk as superscript indicates a quantity at the end of the fracture process zone so that δ_n^* is the normal end-opening and δ_t^* is the tangential end-opening (See Fig. 1). Thus, by measuring J, δ_n^*, and δ_t^* during a series of mixed mode experiments, the potential function Φ can be determined experimentally [29]. In the present approach, both the fracture resistance and the cohesive tractions are defined in terms of the magnitude of the end-openings, δ^*, and the phase angle between the normal and tangential end-openings, φ^*. These two are depicted in Figs. 1(a) and 1(b) respectively, and defined as [14]

$$\delta^* = \sqrt{\delta_n^{*2} + \delta_t^{*2}}, \text{ and } \varphi^* = tan^{-1}\left(\frac{\delta_t^*}{\delta_n^*}\right). \tag{3}$$

The potential function proposed to fit the fracture resistance (now written in a cylindrical form), $\Phi(\delta, \varphi)$, is defined in a piece-wise manner using two differentiable functions,

$$\Phi(\delta, \varphi) = \begin{cases} \Phi_{CT}(\delta, \varphi) & for\ 0 < \delta \le \delta_0 \\ \Phi_B(\delta, \varphi) & for\ \delta_0 < \delta < \delta_{ss} \\ \Phi_B(\delta_{ss}, \varphi) & for\ \delta_{ss} \le \delta, \end{cases} \tag{4}$$

where the subscripts CT, and B refer to the crack-tip and bridging region, respectively. The subscripts 0, and ss represent the onset (initiation) and steady-state fracture respectively. Given Φ in cylindrical coordinates, then using the chain rule for differentiation, the cohesive tractions can be expressed as [19]:

$$\sigma_n(\delta, \varphi) = \cos(\varphi)\ \frac{\partial \Phi}{\partial \delta} - \frac{\sin(\varphi)}{\delta}\frac{\partial \Phi}{\partial \varphi}, \tag{5}$$

$$\sigma_t(\delta, \varphi) = \sin(\varphi)\ \frac{\partial \Phi}{\partial \delta} + \frac{\cos(\varphi)}{\delta}\frac{\partial \Phi}{\partial \varphi}. \tag{6}$$

The potential function corresponding to the crack-tip ($0 < \delta \le \delta_0$) is [30]

$$\Phi_{CT}(\delta, \varphi) = C_3\delta^3 + C_2\delta^2 + C_1\delta + C_0, \tag{7}$$

where the terms C_0, C_1, C_2, C_3 are functions of the phase angle φ only. A 3rd degree polynomial was chosen since it describes well the fracture resistance at the crack-tip for all tested phase angles. Similar shapes of the crack-tip fracture resistance (fitting well a 3rd degree polynomial) can be found in other studies [33].

The potential function corresponding to the bridging fracture process zone ($\delta_0 < \delta \le \delta_{ss}$) is [30]:

$$\Phi_B(\delta, \varphi) = \Phi_0 + \Delta\Phi_{ss}\left(\frac{\delta - \delta_0}{\delta_{ss}}\right)^{\zeta}, \tag{8}$$

where Φ_0, $\Delta\Phi_{ss}$, δ_0, δ_{ss}, and ζ are all functions of φ only. The meaning of these parameters is explained in Section 3.4. The partial derivatives of the potential function needed to obtain the mixed-mode cohesive laws (Eq. (5) and (6)) can be found elsewhere [30].

3. Methods

3.1. Materials and DCB specimens

The laminate used for manufacturing the DCB specimens consisted of 20 unidirectional (UD) stitched layers. The backing in all the layers is facing downwards, which means that the laminate is near-symmetric, but it has an asymmetric interface at the midplane. The glass fabrics used were E-1182 Saertex, and the matrix material was a Hexion RIMR 035c epoxy. A Teflon release foil with a thickness of 35 ± 15 μm was placed in the middle interface (see Fig. 2) to introduce an initial crack of an initial length of a_0 = 70 mm. The laminate was processed by vacuum infusion and was consolidated with a cure cycle of 12 h at 40 °C plus 10 h at 80 °C. The overall fibre volume fraction of the laminate was approximately 58% [34]. The elastic properties of the laminate are given in Table 1 where E_1 and E_2 are the Young's moduli in the x_1 (the fibre direction) and x_2 directions respectively, and ν_{12} and ν_{21} are the major and minor Poisson's ratio, and G_{12}, and G_{13} are the shear moduli. The DCB specimens were cut from the laminate parallel to the fibre direction, and the specimens were randomised before labelling/grouping in order to minimise effects from local manufacturing variations. The dimension of the DCB specimens are as follows: Length, L = 500 mm, width, B = 30 mm, and height, $2H$ = 16.9 mm. Metallic end-blocks were glued to the specimen to facilitate the load introduction, and a pair of metallic pins were inserted

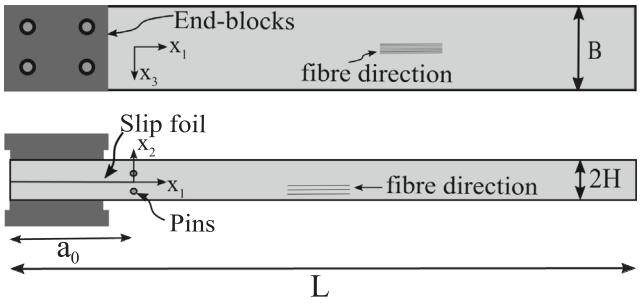

Fig. 2. DCB specimen dimensions.

Table 1
Elastic properties of the UD glass/epoxy laminate [34]. Transversely isotropy is assumed.

E_1	46.3	GPa
$E_3 = E_2$	12.9	GPa
$\nu_{13} = \nu_{12}$	0.26	–
$\nu_{21} = \nu_{31}$	0.07	–
$G_{12} = G_{13}$	4.3	GPa

near the initial pre-crack to mount an extensometer and two linear variable differential transformer (LVDT's) to measure the end-opening displacements. A schematic of the DCB specimen is shown in Fig. 2. Finally, the specimens were also marked using a hand-drawn randomised speckled pattern for digital image correlation measurements.

3.2. Test configuration

The DCB specimen loaded with uneven bending moments (DCB-UBM) can produce stable crack growth for any combination of normal and tangential openings. Furthermore, for such a configuration, the J-integral equation is independent of the crack length and of the details of the cohesive laws. A detailed description of the DCB-UBM test configuration can be found elsewhere [28]; yet, a brief description of the experimental procedure is provided here for the sake of completeness. In the test setup, the DCB specimens are fixed at the uncracked end (opposite side of the initial crack) and loaded at the two beams with uneven bending moments transmitted via the metallic end blocks attached to them. The moments are established by a wired system under tension as shown in Fig. 3(a). The tension load in the wire, P, is the same for both moment arms, however, by using different lever arms, ℓ_1, and ℓ_2 different bending moments M_1, and M_2 are applied on each of the beams at the end of the DCB specimen. This setup allows for any combination of fixed moment ratios (M_1/M_2) i.e., any mixed-mode.

During the test, data was collected by two acquisition systems and two cameras. One of the acquisition systems recorded acoustic emission (AE) data from two sensors, while the other recorded displacements from the extensometer (Δ^E) and the LDVTs (Δ_1^L and Δ_2^L), elapsed time, t, and loads, P_1, P_2, from two separate 2 kN load cells. The two cameras recorded video of the tested specimen; one with a zoom-in on the initial crack and the other with a full view of the specimen. The extensometer (Instron 2620–601, range ±5 mm) measured the linear displacement between the pins, while the LDVTs (RDP GT 5000, range ±5 mm) provided the displacements Δ_1^L, and Δ_2^L. Two AE sensors were mounted on the specimens with a fixed distance of 110 mm between them. The data acquisition frequency was 20 Hz. Fig. 3(b) shows a specimen with all the measurement equipment.

The moments are applied by displacing a lower beam (at a constant displacement rate of 10 mm/min) that is connected to the wiring system as shown in Fig. 3(a). The lever arms are fixed with an initial offset negative angle θ_0 of 10° (after a rotation of 10° the lever arm will be in a neutral horizontal position) in order to counteract the effect of varying moments due to large beam deflections. This variation is presented elsewhere [28]. By staying within the range of ±10° the maximum error on the measurement of the fracture resistance will be smaller than 6% (see [28]). It was observed that for $M_1/M_2 \approx 1$ the beams were deflecting beyond the prescribed limit before reaching steady-state. Therefore, in some tests, the sample was inclined (further rotated) about 10°–14° at the start of the test in order to get the beams within the ±10° limits at the load level where cracking occurred. The test was stopped when the steady-state fracture was reached, which was assumed once the "real-time" value of the applied force remained at a near-constant value.

Table 2
List of the different tested mixed-mode and mode-mixities.

Group	M_1/M_2 [-]	ψ^b [Deg.]	φ^{*a} [Deg.]
1	−1.00	0.0	0.6 ± 1.2
2	−0.66	10.1	3.6 ± 0.5
3	−0.41	19.9	5.6 ± 0.7
4	0.00	40.9	9.1 ± 1.3
5	0.12	47.8	10.2 ± 0.12
6	0.50	68.9	24.2 ± 1.9
7	0.81	83.1	52.6 ± 2.9
8	0.87	85.4	69.45 ± 2.9
9	0.87	85.4	51.7 ± 14.4
10	0.96	88.7	45.5 ± 9.5
11	0.99	89.7	65.7 ± 3.08

[a]The values are the average of the 4 tests carried at the same nominal phase angle ψ.
[b]Analytical solution for an orthotropic DCB-UBM specimen [35].

3.3. Data analysis

The full experimental campaign consisted of 44 tested specimens in total. These tests were divided into 11 different groups with 4 specimens per group. Each group was tested at different moment ratios to cover the entire range of mixed-modes (from pure normal opening, $M_1/M_2 = -1$, to near pure tangential opening, $M_1/M_2 = 0.99$). A list of the tested groups is given below in Table 2. The tested specimens are grouped by the applied moment ratio M_1/M_2, with the corresponding nominal phase angle (the LEFM phase angle formed by the stress intensity factors K_I and K_{II}) ψ [35], as well as the average measured end-opening phase angle φ^* for each group.

The analytic solution for the J-integral evaluated along the external boundaries of a DCB-UBM specimen for plane strain is [29]

$$J = \frac{21(M_1^2 + M_2^2) - 6M_1M_2}{4B^2H^3E_1^*} \tag{9}$$

where M_1 and M_2 are the external bending moments ($M_1 = P\ell_1$, $M_1 = P\ell_2$), and E^* is the Young's modulus for plane strain[1,2] ($E_1^* = E_1/(1-\nu_{12}\nu_{21})$).

3.4. Extraction of fracture and fitting parameters

The overall process of measuring the parameters needed to determine the mixed-mode cohesive laws of a material based on the proposed method is shown schematically as a series of steps in Fig. 4.

Steps 1 and 3 in Fig. 4 are conceptually straightforward. The experimental R-curves, i.e. Step 1, are obtained by the fracture mechanics tests described above, and the calculation of the fracture resistance, $J_R(\delta^*, \varphi^*)$, (from Eq. (9), and Appendix A of [29]). For Step 3, once the

[1] Since the beams are under bending moment, the flexural modulus might be more appropriate than the elastic modulus

[2] Plane strain was chosen because, during crack initiation, the crack tip stress field is seen as being a wide specimen. However, it can be argued that the beams of the specimen are slender and thus plane stress would be more appropriate. The difference between these two is small.

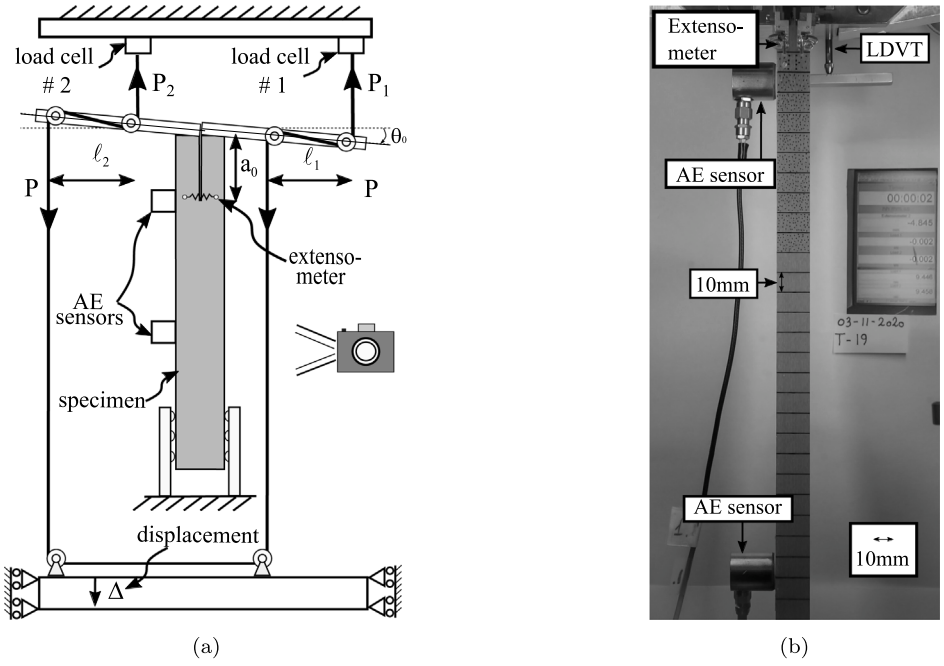

Fig. 3. DCB-UBM test set-up and measurement equipment (a) schematic (b) picture of mounted specimen.

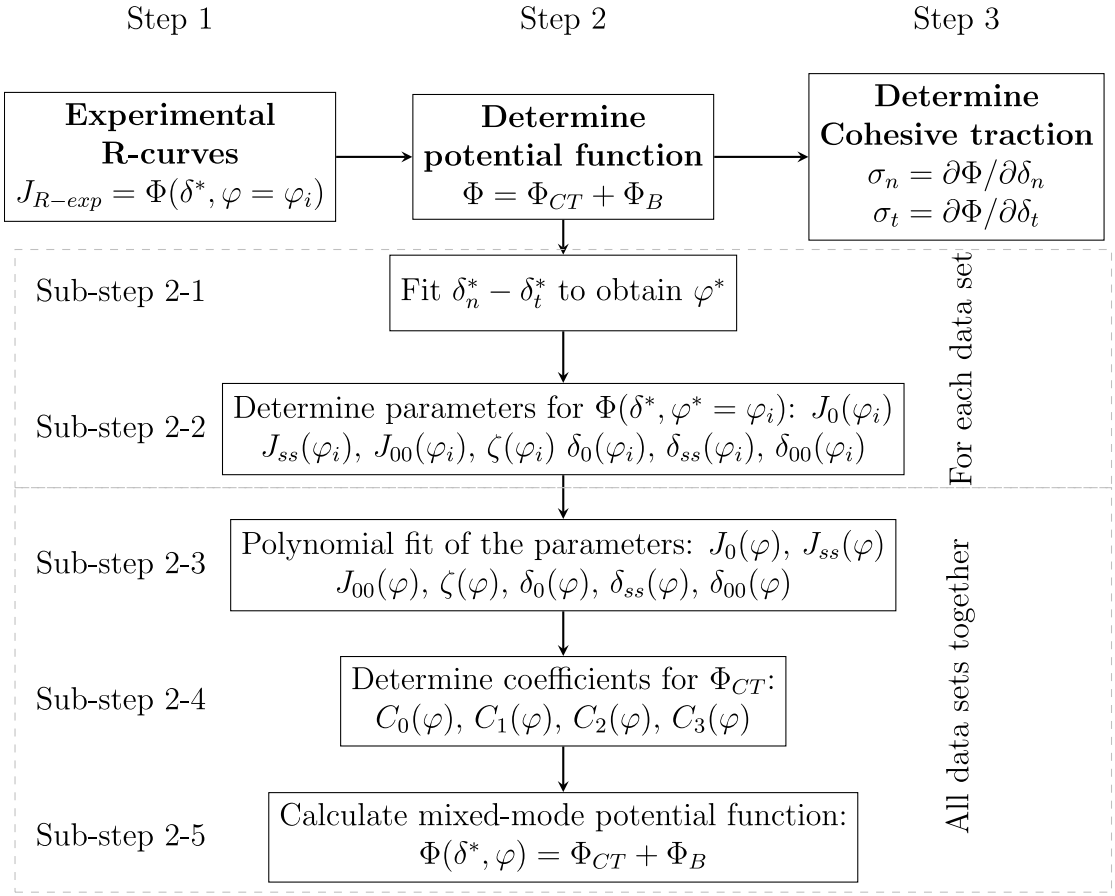

Fig. 4. Overview of the proposed method for extracting mixed-mode cohesive laws from experimental R-curves. The subscript i refers to the measured value of test number i.

potential function Φ has been determined, then the cohesive tractions are obtained using Eqs. (5) and (6). The determination of the parameters for the potential function involves several steps as described in Fig. 4. First, the parameters to determine the potential function need to be extracted individually for each data set (i.e. for a fixed φ^* for each test). This process is divided into two sub-steps (Sub-step 2–1 and Sub-step 2–2). Once the fracture parameters have been determined for each data set, then all data sets are connected to map the potential

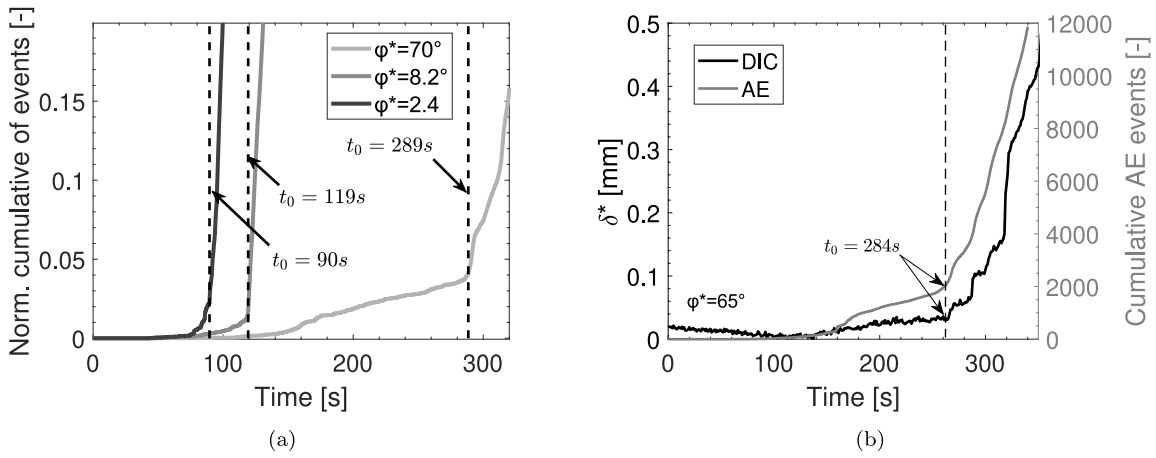

Fig. 5. (a) Cumulative of AE events as a function of time elapsed for determination of crack initiation t_0 and (b) comparison between t_0 from AE (cumulative events) and end-opening displacements from DIC measurements.

function in the φ^*−direction using fitting functions computed for each parameter. This is, again, broken down in 3 Sub-steps (Sub-step 2–4 to Sub-step 2–6). A detailed description of each sub-step is provided below.

3.4.1. Extraction of parameters for an individual data set

Sub-step 2–1 involves the determination of the average phase angle of the end-openings φ^*. This is done using a linear fit of δ_n^* and δ_t^*. The slope from the linear fit is used in combination with Eq. (2) to calculate the average phase angle, φ_i^*, for each experiment (subscript i indicates the experimental number). Fig. 6(a) shows an example of Sub-step 2–1. In Sub-step 2–2, several fracture parameters that describe $\boldsymbol{\Phi}(\delta^*, \varphi^* = \varphi_i)$ are extracted from the R-curves (listed in Fig. 4). First, the initiation of the crack, and the steady-state crack growth should be identified. In principle crack initiation can be identified visually using high magnification cameras, however, in practice, it can be difficult to identify the onset of crack growth due to the very small openings at the crack-tip; furthermore, cracking can start in the middle of the specimen ($x_3 = 0$), and a curved crack front starts developing (not uniformly along the width of the specimen) so that the initial crack growth may not be visible from the surface that is being recorded ($x_3 = H/2$). For this reason, in the present study, AE measurements were used to determine the time of crack initiation, t_0, which is then correlated to the load (and hence to J_0, and δ_0) at that time. More precisely, the time of crack initiation, t_0, is determined from the cumulative sum of AE events, which shows a characteristic "knee" that depicts a shift from a low to a higher activity. This time is then taken as an indication of crack initiation. The approach is shown in Fig. 5(a), where the cumulative of AE events are plotted for 3 different experiments with different phase angle values. To corroborate these results, cumulative events from AE measurements were overlapped with DIC measurement of end openings as shown in Fig. 5(b). Both measurements provide a similar time of crack initiation.

Steady-state crack growth is attained when the bridging zone is fully-developed. The transition to a steady state is defined from the R-curves as the instance when the fracture resistance attains either a constant value or when it starts oscillating around a constant value. Steady-state corresponds to the coordinate (δ_{ss}, J_{ss}) in the R-curves. In practice, however, a criterion needs to be defined to systematically determine the end-opening corresponding to the steady-state fracture resistance. In the present work, the maximum value of J_R (within the valid range of the lever-arms angle as mentioned in Section 3.2) was taken as steady-state, so that steady-state value J_{ss} corresponds to the maximum value of J_R and its corresponding end-opening, (δ_{ss}). An example of the identification of crack initiation and steady-state is illustrated in Fig. 6(b). Then, the shape parameter, ζ, is obtained by fitting the experimental R-curve (black curve) to Eq. (8).

To complete Sub-step 2–2, the parameters δ_{00} and J_{00} (which are explained in detail in [30]) need to be identified in order to determine the values of $C_0 - C_3$ (explained below). The parameters δ_{00} and J_{00} correspond to the inflexion point of $\boldsymbol{\Phi}_{CT} = (0 < \delta < \delta_0, \varphi_i)$, which can be obtained by means of ordinary derivatives of $\boldsymbol{\Phi}_{CT} = J_{CT}$ [30].

3.4.2. Parameter fitting of all data sets together

Having determined δ_{00} and J_{00} for all sets individually, Sub-step 2–3 consist of connecting all parameters (i.e. J_0, $J_s s$, J_{00}, δ_0, δ_{ss}, δ_{00}, and ζ) data sets (different φ^*'s) together using polynomial fitting. Next, in Sub-step 2–4, the functions $C_0(\varphi^*) - C_3(\varphi^*)$ are determined. These functions are obtained using the polynomial fits of δ_0, J_0, δ_{00}, and J_{00}, which are continuous functions dependent on φ^*. This means that a unique set of coefficients $C_0(\varphi^*) - C_3(\varphi^*)$ can be found at any given φ^* [30]. Finally, in Sub-step 2–5 the complete potential function is obtained by adding the potential function of the crack-tip and the bridging potential function to ensure continuity of $\boldsymbol{\Phi}$ between $\boldsymbol{\Phi}_{CT}$ and $\boldsymbol{\Phi}_B$.

4. Results

4.1. Overview of results

The normal and tangential end openings for representative experiments are plotted in Fig. 7(a). From Fig. 7(a), it can be seen that the end-openings are indeed increasing nearly proportional to each other giving a fairly constant value of φ^* from the crack initiation to the steady-state (fully developed bridging zone). R-curves of the same representative experiments are shown in Fig. 7(b). Overall, the J-integral value increases rapidly to J_0 for very small end-openings values, which corresponds to crack initiation. Then, beyond J_0, J_R increases more slowly until reaching J_{ss} for much larger values of end-openings. Some of the experiments with high phase angle values did not reach steady-state; the end-points of the linear fits of these experiments are indicated by an open symbol and an arrow in Fig. 7. A previous study had encountered similar issues reaching steady-state for experiments with high phase angle values [29]. Plausible reasons for this are further discussed in Section 5. From Fig. 7(b), it can be seen that for a fixed δ^* value, the fracture resistance varies significantly as a function of the phase angle φ^*. For small φ^* values, the R-curves show a strongly non-linear behaviour, rising quickly and then flattening out reaching a steady state. For large φ^* values, after rising quickly the fracture resistance increases almost linearly until reaching a steady state value.

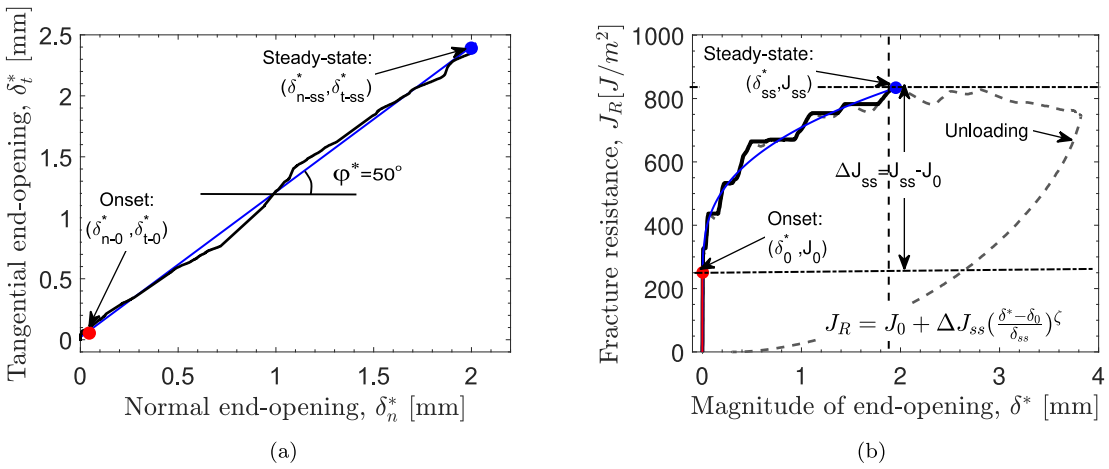

Fig. 6. Example for (a) Sub-step 2-2: determination of phase angle from a linear fit of δ_n^* and δ_t^* measurements and (b) Sub-step 2-3: Determination of fracture parameters using the experimental R-curve. The red circle indicates crack initiation, while the blue circle indicates steady-state. The red curve indicates the crack-tip region, while the blue indicates the bridging zone.

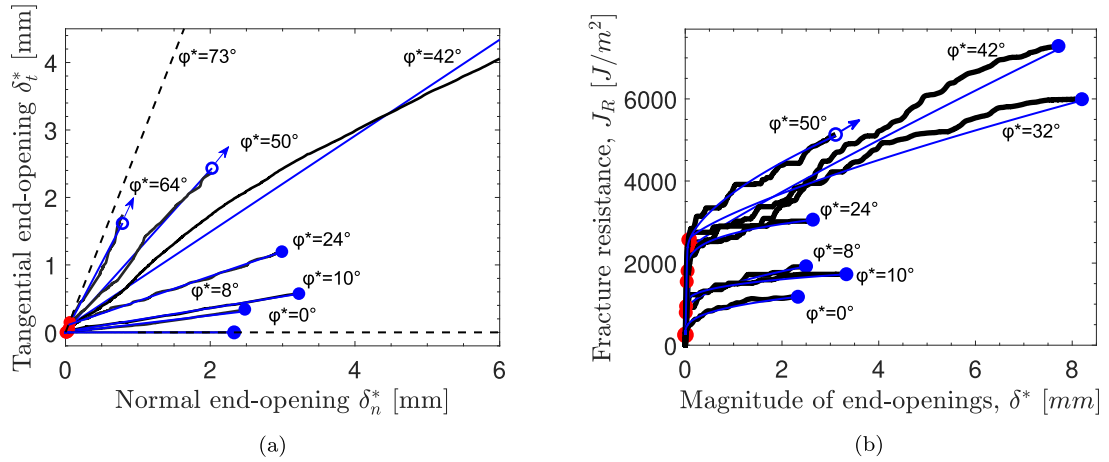

Fig. 7. Plots of representative (a) end-openings at different mixed-mode loading and (b) R-curves at different phase angles. The experimental data are shown in solid black, while the fitted data are in blue curves for each experiment. The red circles indicate crack initiation, while the full-blue circles indicate the onset of steady-state. The open circles with an arrow indicate that steady-state was not reached. The dashed lines in (a) indicate the range covered in the present experimental campaign.

4.2. Interpolation of fracture and fitting parameters

The measurements of the fracture parameters (listed in Sub-step 2–4) and the corresponding fitting functions are presented in Figs. 8 to 11. In these figures, the grey area enclosed by the black dashed curves represents the 95% confidence intervals. All parameters, but the shape function, are fitted using polynomial fits (either least-squares or Gaussian process models [36]). The degree of the polynomial fits was chosen based on two criteria; (i) best fit in terms of the R^2 value, and (ii) that the interpolation does not produce any results that are not physically sound, e.g. negative values of fracture resistance.

In Fig. 8, the parameters δ_{00} and J_{00} are shown. Because of the small openings at the crack-tip, fitting of δ_{00} can lead to negative openings at some values of φ. To avoid such nonphysical values, the logarithm of δ_{00} was used in the fitting instead of the δ_{00} value. This also provided higher R^2 values. Fig. 8(b), shows the corresponding fracture resistance values and the polynomial fit. The same approach of the logarithm was used for δ_0 in Fig. 9(a). For J_0, the polynomial fit was carried out using Gaussian process models [36]. The fracture parameters at steady-state are shown in Fig. 10(a) for the fully-developed end-openings and in Fig. 10(b) for the fracture resistance. The error bars shown in the plot for J_0 and J_{ss} are calculated to account for geometrical variations of the width and height of the specimen and to account for the small change of the effective lever-arm(s) as these rotate following the beams of the DCB specimen. Note that only valid experiments are shown, which means that those experiments that did not reach steady-state are not included, hence the different number of experiments in Figs. 8–9, and Fig. 10.

The experimental values of the shape parameter ζ, and its fitting function are shown in Fig. 11(a). An S-shaped function was used to fit ζ instead of a polynomial function (see Appendix B). The coefficients $C_0 - C_3$ normalised by the corresponding maximum value are shown in Fig. 11(b). The coefficients describe the variation of the fracture resistance in the crack-tip region.

The vast majority of the experimental data points lay within the 95% confidence interval. Furthermore, the R^2 values of the fits range from 0.48 to 0.97. In general, there is a considerably larger scatter in the steady-state parameters. This is further addressed in Section 5. Note that the largest attained phase angle was $\varphi^* = 73°$, as such, any value result beyond this value is the result of extrapolation. The same applies to the computed potential function, and the cohesive laws derived from it.

4.3. Mixed-mode fracture resistance

A surface plot of the potential function $\Phi(\delta_n, \delta_t)$ is shown for the crack-tip and the bridging zones in Fig. 12. Representative R-curves (as

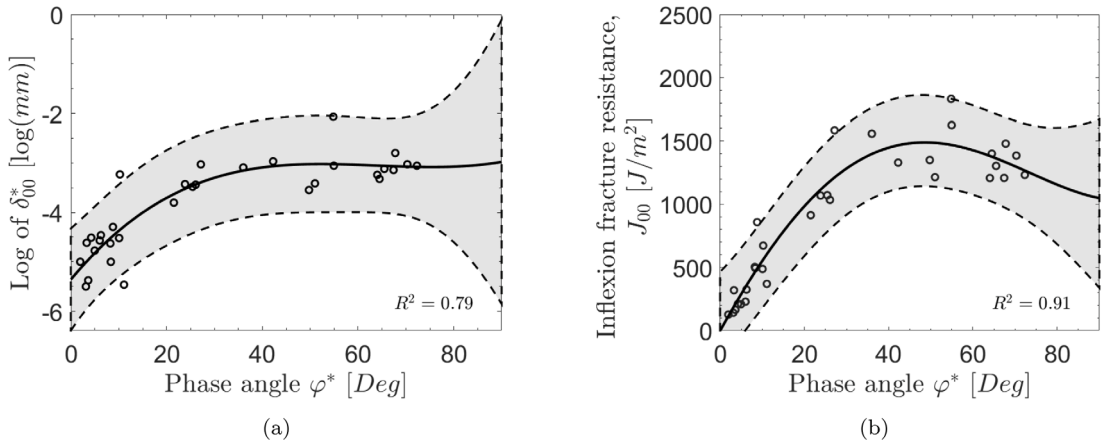

Fig. 8. Interpolation of the fracture parameters (a) $\delta_{00}(\varphi^*)$ and (b) $J_{00}(\varphi^*)$.

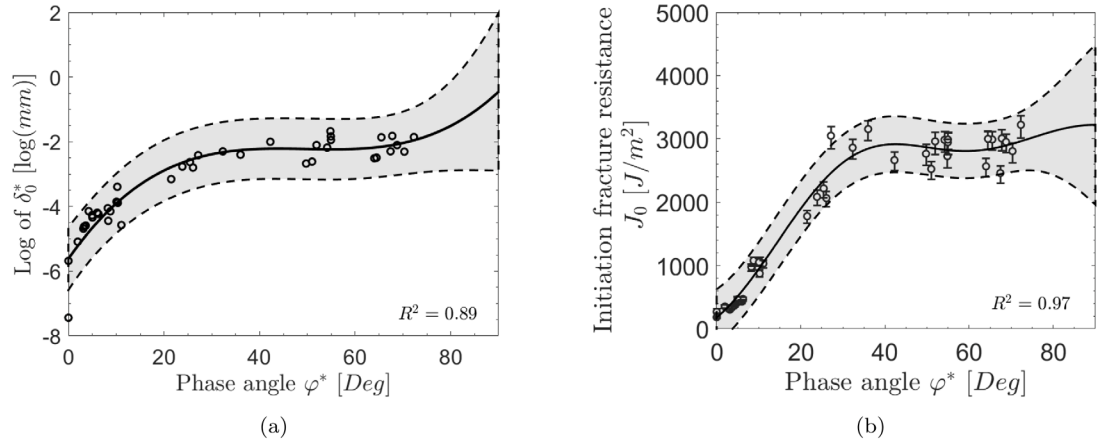

Fig. 9. Interpolation of fracture parameters related to crack initiation (subscript 0) (a) $\delta_0(\varphi^*)$ and (b) $J_0(\varphi^*)$.

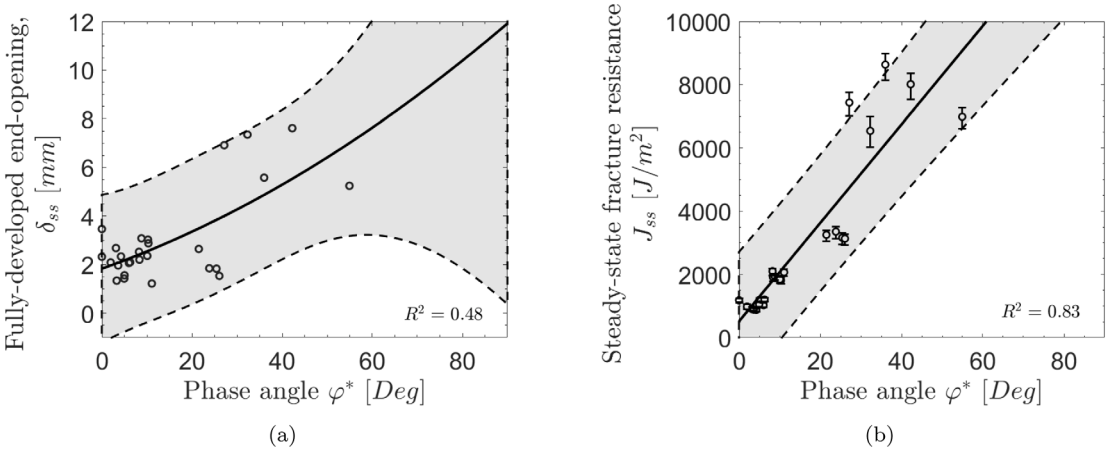

Fig. 10. Interpolation of fracture parameters related to steady-state crack growth (subscript *ss*) (a) $\delta_{ss}(\varphi^*)$ and (b) $J_{ss}(\varphi^*)$.

a function of the normal and tangential end-openings) are shown in the same plots for comparison.

It can be observed that, overall, there is a very good agreement between the potential function and the measured R-curves. The difference between Φ and the J_R curves varies slightly with different phase angles; however, overall there is a small difference for all tested coupons.

4.4. Mixed-mode cohesive tractions

The 3D mixed-mode cohesive tractions σ_n and σ_t are shown as a function of δ_n and δ_t in Fig. 13, and Fig. 14. In Fig. 13 the axes are chosen so that the shape of the cohesive tractions at the crack-tip can be appreciated. The plots of the crack-tip of the normal traction in

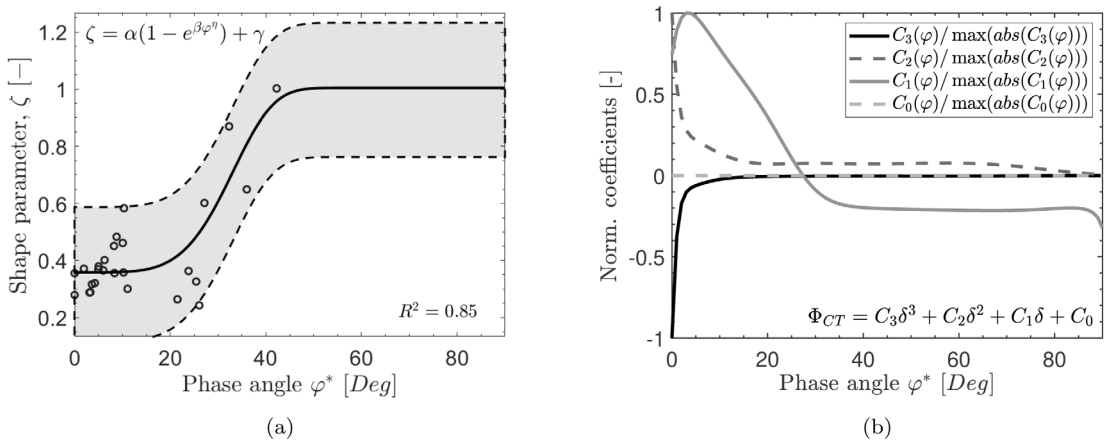

Fig. 11. Interpolation of (a) shape parameter ζ for Φ_B and (b) the coefficients of Φ_{CT}.

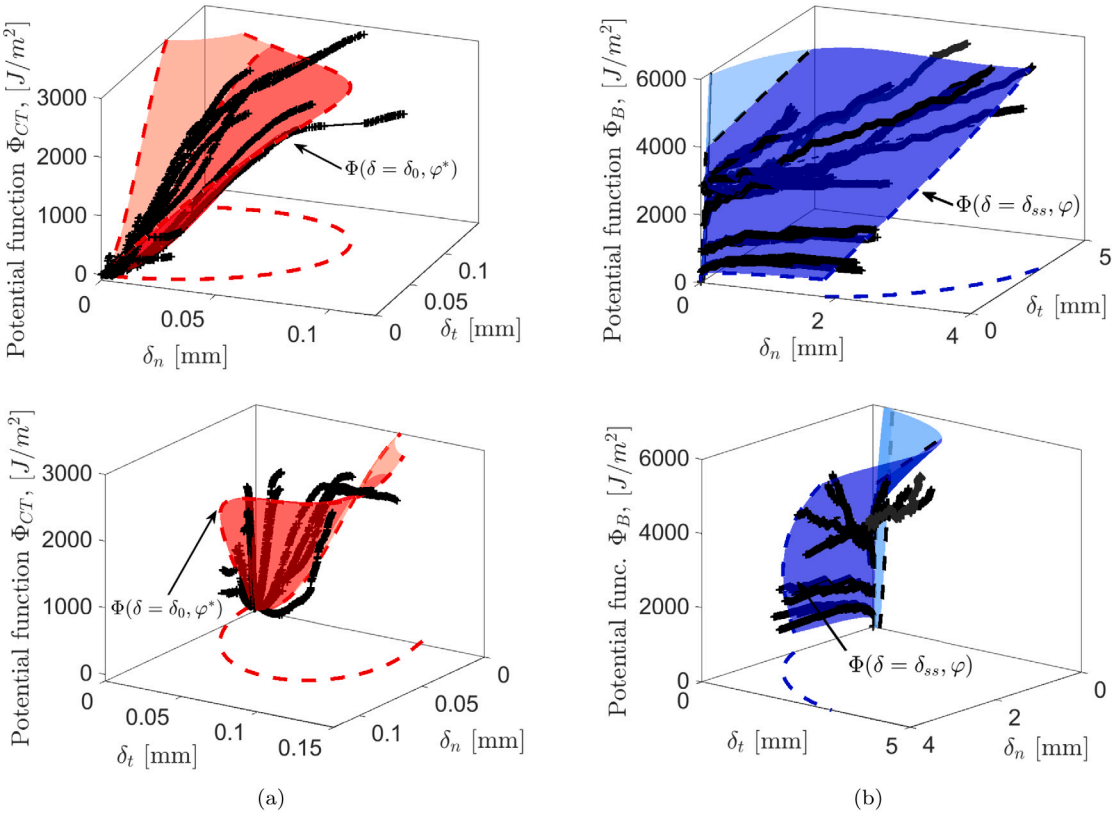

Fig. 12. Comparison between Φ (surface) and J_R (curves) showing (a) the crack-tip region (red), and (b) the bridging region (blue). The upper and lower plots show the same data, however, with a different view. The regions with a lighter colour (red/blue) represent the range of the potential function which comes from extrapolation. The dashed curves are the values of Φ evaluated at δ_0 (for red) and δ_{ss} (for blue) as well as their projection onto the $\delta_n - \delta_t$ plane.

Fig. 13(a), show a peak traction value $\hat{\sigma}_n$ of about 61 MPa at very small end-openings (about 5μm) rapidly decreasing as δ^* increases. The crack-tip area of the shear traction in Fig. 13(a) shows a more rounded shape with a peak shear traction value $\hat{\sigma}_t$ of about 41 MPa at relatively large values of δ_t (up to 70 μm). The normal and shear tractions show not only different peak values but very different shapes. Clearly, both σ_n and σ_t depend on both δ_n and δ_t, i.e. the derived mixed-mode cohesive laws are coupled. It can be noted in Figs. 14 and 13(a) that for small tangential dominated openings ($0 < \delta < 10$ μm and $\delta_n \approx 0$) σ_n shows negative values (down to ≈ -5 MPa). Likewise, σ_t takes a negative value (-12 MPa) for small openings. The cohesive tractions are plotted in Fig. 14 for the full opening range with a truncation in the traction axis to observe the shape (and extent) of the cohesive tractions in the bridging region. In the bridging region ($\delta_0 < \delta < \delta_{ss}$), both the normal and tangential bridging tractions are dependent on the phase angle with a small value at $\varphi = 0°$, and a larger value at $\varphi = 90°$.

For a more descriptive and easier interpretation, the obtained cohesive tractions are plotted in Fig. 15 for selected phase angle values. The thin dashed black curve in Figs. 15(a) and 15(a) shows the discontinuities obtained at the transition point (δ_0). Large variation of the cohesive tractions can be observed for different phase angles. From Figs. 15(c) and 15(d) it can be seen that the maximum value of peak normal traction, $\hat{\sigma}_n$, occurs at a phase angle of $\varphi = 4°$, and the maximum value of peak cohesive shear traction, $\hat{\sigma}_t$, occurs at $\varphi = 70°$.

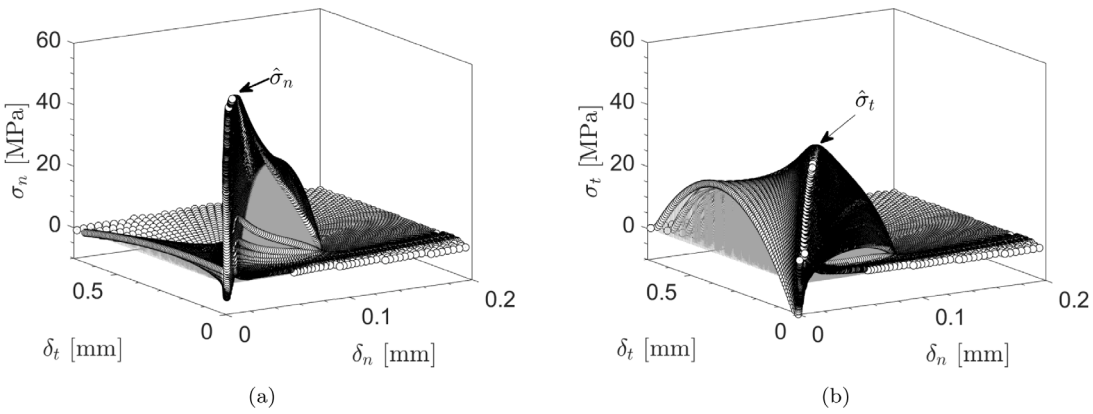

Fig. 13. 3D plots of the cohesive tractions as a function of δ_n and δ_t with a focus on the crack-tip region for (a) σ_n and (b) σ_t.

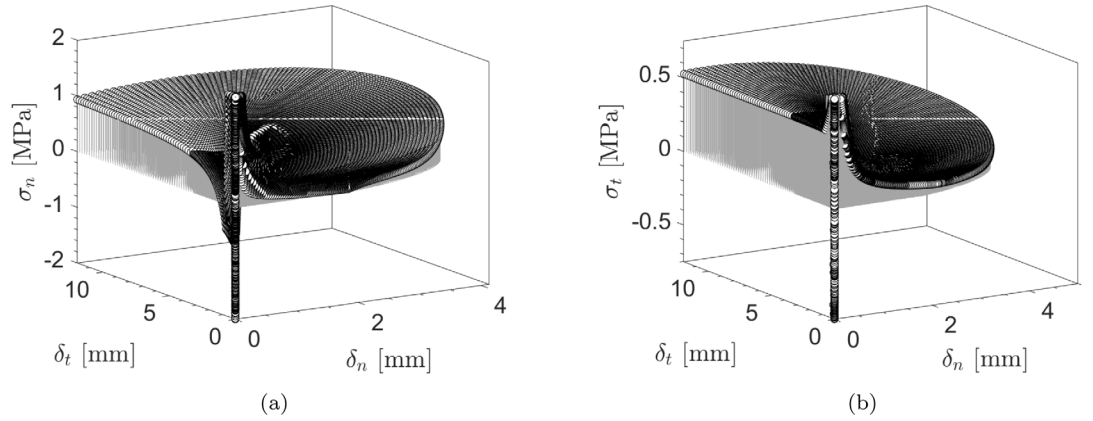

Fig. 14. 3D surface plots of the cohesive tractions as a function of δ_n and δ_t. The traction axis is cut-off to visualise the shape of the bridging (a) σ_n and (b) σ_t.

5. Discussion

Some key results from the experimental campaign and extracted cohesive laws are further discussed in this section.

5.1. Characteristics of cohesive tractions

The present work provides experimental data suggesting that cohesive tractions are coupled for all mixed-mode conditions. Non-zero normal tractions are found under pure tangential opening displacement (Figs. 13 and 14). This result is in agreement with the findings of an earlier study [29]. Sørensen and Goutianos associated this effect with interface dilatation [37], and they have suggested three physical phenomena that may lead to it namely (i) in-plane surface roughness (ii) shear cracks (formed at an angle with respect to the main crack plane) and (iii) fibre buckling. Interface dilatation is also known from the fracture of concrete [38]. Likewise, non-zero shear tractions are obtained for pure normal separations. The proposed approach is rather general in the sense that it makes no assumptions with regard to the coupling of the tractions. The method aims to describe the fracture resistance as close as possible, and the cohesive tractions are then derived from it.

It is therefore appropriate to discuss what constraints should be enforced for the potential function and cohesive tractions. The presence of normal tractions under pure tangential opening displacements (see Fig. 15(a)) and especially the presence of non-zero shear traction under pure normal opening (see Fig. 15(b)) may appear surprising at first. However, these non-zero traction values cannot be disregarded by the use of symmetry arguments. If the fracture plane is not strictly symmetric (as in the present case, see Section 3.1), then the symmetry arguments used to define pure modes (in LEFM) cannot be applied (M.D. Thouless, private discussion). The specimens used in the present study are nominally symmetric (10 UD layers above and below the mid-plane), but have an asymmetric mid-plane interface due to the orientation of the backing. As mentioned previously all the specimens were manufactured and tested with the backing facing downwards as depicted in Fig. 16. The presence of backing bundles perturbates the crack tip stress field inducing asymmetry which can cause the crack to kink off of the specimen mid-plane (and into the backing bundles). It remains unclear to the authors whether this would be enough to produce shear tractions measurable at macroscopic specimens, however, since the symmetry argument is cannot be applied, then there is no reason to enforce a zero shear traction under pure normal separations.

The surfaces of the normal and shear tractions (Figs. 13(a) and 14(b)) have distinctively different shapes. The surface of the normal traction has a slender shape with its peak value at small openings and small phase angle values. Under pure normal opening, the material in the FPZ fails due to tension which usually gives a small FPZ (low values of δ_0). This leads to a more "brittle" fracture behaviour with a steep raise, followed by a drop-off of the cohesive tractions. The surface of the shear traction has a more "plumped" shape with peak traction located at $\varphi = 70°$. It is well known that as the proportion of shear loading is increased, then the fracture process zone ahead of the crack tip starts to develop multiple microscopic shear cracks (cusps) [39]. This results in a longer crack-tip FPZ which corresponds to larger values of δ at the crack-tip before starting the bridging region (the red curves in Figs. 14(a) and 14(b) extend longer as φ increases).

Large differences can also be observed between normal and shear tractions in the bridging region. Micromechanical models of cross-over bridging ligaments produce coupled normal and shear tractions with

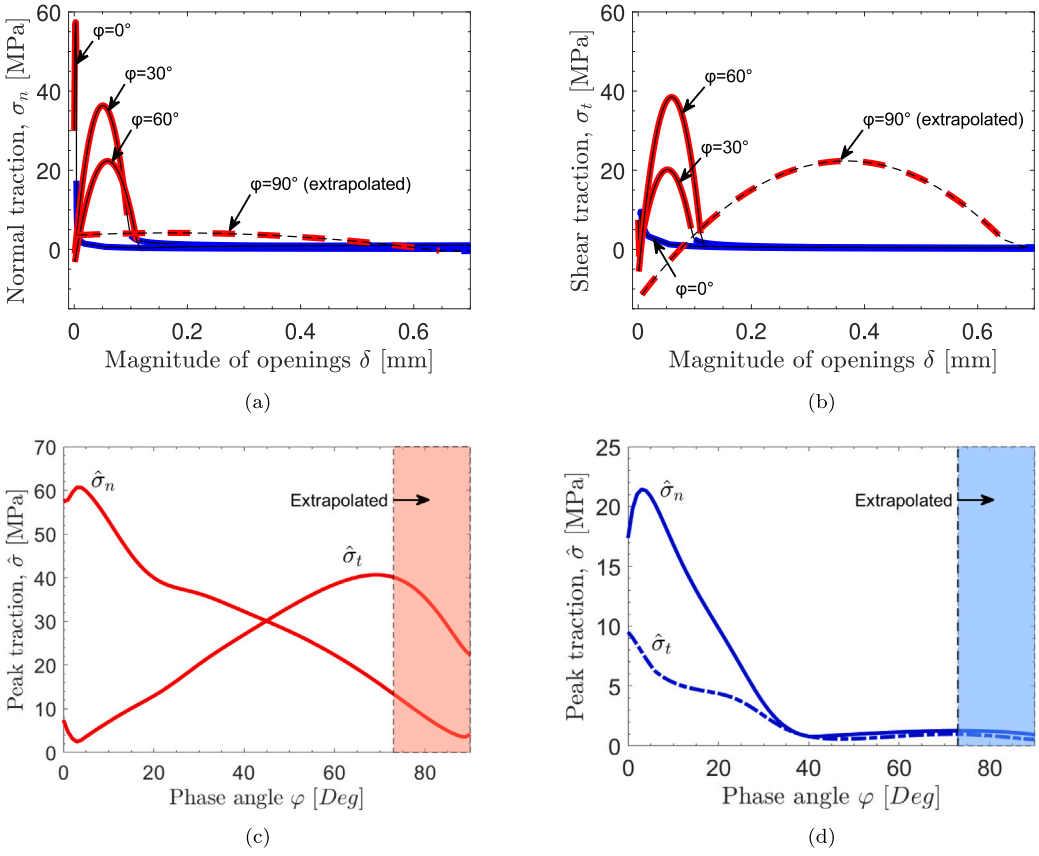

Fig. 15. Cohesive tractions evaluated on intervals of 30° of the phase angle φ for (a) normal traction and (b) shear traction. Peak cohesive tractions, $\hat{\sigma}_n$, $\hat{\sigma}_t$ as a function of the phase angle in (c) the crack-tip and (d) the bridging region. The red curves represent the tractions in the crack-tip region, whereas the blue curves indicate the cohesive tractions in the bridging region.

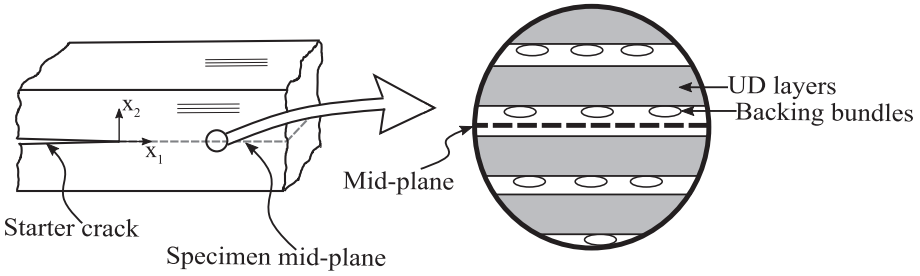

Fig. 16. Schematic of a specimen (macroscopic) with symmetric laminate but asymmetric interface (microscopic).

different shapes [40,41]. The obtained normal bridging tractions found in the present study are larger than the shear bridging tractions, which is in contrast to these micromechanical predictions. It is possible that, under mixed-mode and pure tangential displacement opening, some of the bridging fibres will be under compression and buckle, and thus not contribute much to the bridging tractions.

5.2. Model limitations and assumptions

There are two major assumptions of the present work. The first one is that the cohesive tractions can be derived from a potential function Φ. This assumption implies that the cohesive traction is independent of the history of the crack-opening displacements. This assumption is implicit for all potential-based mixed-mode cohesive laws. Although a micromechanical model (small displacements, small rotations) gives mixed-mode cohesive laws that are derived from a potential function [41] when fibre buckling and fibre failure are disregarded, it still remains an open research question if the cohesive laws due to fibre bridging are path-dependent. The second assumption made in the present work is that the end-openings increase proportionally. It can be seen (Fig. 7(a)) that this is a good approximation for most of the opening range. However, larger deviations are expected for very small openings where the size of the active cohesive zone is small (within the K-dominated zone, φ can be expected to be controlled by ψ). From [42] it can be shown that under LEFM conditions the phase angles of the openings at the crack-tip are related to ψ as

$$\tan(\varphi) = \lambda^{1/2} \tan(\psi) \tag{10}$$

where $\lambda = E_2/E_1$. However, this needs to be further studied with more precise measurements of the crack tip opening displacements.

In principle, the proposed method should be applicable to any non-linear time-independent material/interface regardless of the size of the FPZ. The method is robust in the sense that by adapting the functional form of the potential function, different damage mechanisms should be

represented accurately. Future work could be the implementation of the method to other materials/interfaces involving large fracture process zone, e.g. debonding of adhesive joints.

5.3. Fitting of parameters

As mentioned earlier the maximum attained measured phase angle value is $\varphi^* \approx 73°$ even under load ratios of $M_1/M_2 \approx 1$ ($\psi \approx 90°$). As such, any conclusion made for $\varphi^* > 70°$ is derived from the extrapolation of data.

The correlation of the fracture process parameters gives good to an excellent agreement based on the R^2 values. In general, more scatter was observed for the correlation of parameters at the steady-state point, particularly for tangential-dominated openings. One of the reasons is that there is less data as not all of the experiments reached steady-state. Another reason is that, unlike crack initiation, there is no standardised approach to determining a steady-state. At small openings ($\delta < 80\mu$) the shear traction for $\varphi^* = 90°$ comes out negative (Fig. 15(b)). This is clearly non-physical as it would produce negative work for $0 < \delta < 80$ μm. We believe this is an artefact of the fitting approach.

The fitting carried out was done in such a way that the potential function was separated into functions of δ and functions of φ. In this way, instead of doing fitting of two independent variables [29], the fitting is first carried out using only one variable. Next, to interpolate the parameters as a function of φ^* polynomial functions (for all except the shape parameter) were used due to their simplicity. Furthermore, polynomials are flexible and they do not enforce a monotonic increment of $J_0(\varphi^*)$. Non-monotonic variation of the J_0 value as a function of the mixed-mode has been observed [43]. The authors see no physical justification to enforce a monotonic increase in J_0 from pure normal to pure tangential opening displacement, as required by the commonly used BK criterion [44].

In the proposed work, 11 groups of different nominal mode-mixities were tested. Clearly, the more tested mixed-modes, the better the cohesive tractions will be described. However, in principle, the proposed method only requires $n+1$ different nominal mixed-mode values (if n is the highest polynomial degree used to fit the fracture parameters). For the present interface, the largest polynomial degree was 5th so only 6 different nominal mixed-mode values should suffice. This represents a reduction of the required experiments in comparison with the method which required at least 8 sets of J_R data (different φ^*) [29], while also eliminating the wobbling effect observed for that approach.

5.4. Experimental limitations

In the present study, a uniform crack front is assumed and the end-openings are measured from the specimen's edge. However, if the beam experiences anticlastic behaviour then the crack front will not be uniform [45,46]. This is currently not accounted for in the data analysis of the present study. A way to address this experimentally is to reduce the width of the fracture process zone (e.g. by introducing symmetric side groves) or reduce the specimen width [46]. Another experimental limitation is that there might be friction between the crack faces for pure tangential opening displacements (i.e., $M_1/M_2 = 1$). In the present study, this was partially addressed by not prescribing moment ratios of 1, but slightly lower values (i.e., $M_1/M_2 = 0.99$) to avoid the contact of the two beams. Still, this issue deserves more attention, since the fracture surfaces are found to be non-planar.

The authors would like to give a word of caution on the conclusions made on the crack tip behaviour particularly on the obtained negative normal and shear tractions at small openings (see Fig. 15). The magnitude of the negative normal and shear tractions is 5 MPa and may be within the uncertainty of the method. A more detailed study should be conducted to clarify if these findings are correct.

6. Conclusion

A general procedure to determine the mixed-mode cohesive laws based on parameters extracted from experimental R-curves is presented. The implementation of the method was carried out using a UD composite laminate which exhibited large-scale fibre bridging. It was found that a large portion of the total energy dissipated (30–85 %) during crack growth corresponds to the work of the bridging tractions. This means that ignoring fibre bridging may lead to large inaccuracies in the prediction of the load-carrying capacity of structures. The experimental results provide evidence of coupled cohesive laws. Furthermore, the approach enables separate cohesive laws for the crack-tip (high traction values ≈ 30–60 MPa, small separations ≈ 10–100 μm) and bridging (low traction values ≈ 20 MPa, large separations ≈ 3–8 mm). Such a description is more realistic than the state-of-the-art idealised cohesive laws.

CRediT authorship contribution statement

R. Erives: Conceptualization, Methodology, Data curation, Formal analysis, Writing – original draft. **B.F. Sørensen:** Conceptualization, Supervision, Writing – review & editing. **S. Goutianos:** Methodology.

Declaration of competing interest

The authors declare that they have no known competing financial interests or personal relationships that could have appeared to influence the work reported in this paper.

Data availability

Data will be made available on request.

Acknowledgements

The present article was partially funded by the Mexican National Council on Science and Technology, and the Energy Sustainability fund (CONACyT-SENER), and the RELIABLADE project supported by the Danish Energy Agency through the Energy Technology Development and Demonstration Program (EUDP), grant no. 64018-0068. The authors would like to acknowledge Helmuth L. Toftegaard for cross-checking parts of the experimental analysis.

Appendix A. Experimental data: fracture parameters

The fracture mechanics parameters are summarised in Table 3.

Appendix B. Fitting of fracture parameters

The coefficients of the fracture parameters are listed in Table 4:

The shape function $\zeta(\varphi)$ (Fig. 11(a)) was fitted using the equation

$$\zeta(\varphi) = \alpha(1 - e^{\beta\varphi^{*\eta}}) + \gamma \tag{11}$$

with $\alpha = 0.6451$, $\beta = -2.563E-08$, $\eta = 4.932$, $\gamma = 0.3524$.

Appendix C. Supplementary data

Supplementary material related to this article can be found online at https://doi.org/10.1016/j.compositesa.2022.107346.

Table 3
Experimental data.

φ^* [Deg]	J_0 [J/m^2]	J_{ss} [J/m^2]	δ_0 [mm]	δ_{ss} [mm]	ζ [−]	δ_{00} [mm]	J_{00} [J/m^2]
0.0	269	1180	0.0006	2.33	0.36	NA[a]	NA[a]
0.0	183	1174	0.0034	3.47	0.28	NA[a]	NA[a]
1.9	353	978	0.0062	2.09	0.37	0.0067	126
3.1	303	923	0.0092	2.68	0.29	0.0041	141
3.3	332	894	0.0098	1.34	0.29	0.0099	319
3.6	337	881	0.0101	1.97	0.32	0.0046	164
4.2	369	874	0.0158	2.34	0.32	0.0110	211
5.0	467	1046	0.0139	1.43	0.37	0.0085	208
5.0	418	1192	0.0130	1.56	0.38	NA[c]	NA[c]
6.0	430	1026	0.0150	2.07	0.37	0.0104	228
6.3	471	1202	0.0144	2.10	0.40	0.0116	324
8.2	978	2100	0.0173	2.53	0.45	0.0098	503
8.3	961	1910	0.0117	2.21	0.36	0.0067	494
8.8	1078	1946	0.0157	3.08	0.48	0.0136	858
10.1	1053	1843	0.0211	2.36	0.46	0.0109	487
10.2	891	1624	NA[b]	NA[b]	NA[d]	NA[b]	NA[b]
10.2	873	1843	0.0335	3.03	0.36	0.0395	672
10.3	1058	1816	0.0204	2.88	0.58	NA[c]	NA[c]
11.1	1031	2067	0.0103	1.22	0.30	0.0042	369
21.5	1777	3252	0.0424	2.65	0.26	0.0223	913
23.8	2083	3353	0.0625	1.85	0.36	0.0325	1069
25.4	2216	3160	0.0719	1.83	0.33	0.0308	1071
26.1	2063	3132	0.0607	1.54	0.24	0.0321	1034
27.1	3049	7435	0.0891	6.92	0.60	0.0484	1585
32.3	2861	6544	0.1002	7.35	0.87	NA[c]	NA[c]
36.0	3155	8634	0.0904	5.58	0.65	0.0455	1558
42.3	2664	8015	0.1350	7.62	1.00	0.0515	1329
49.8	2765	NA[d]	0.0687	NA[d]	NA[d]	0.0288	1350
51.0	2523	NA[d]	0.0730	NA[d]	NA[d]	0.0330	1214
51.9	2961	NA[d]	0.1216	NA[d]	NA[d]	NA[c]	NA[c]
54.2	2984	NA[d]	0.1127	NA[d]	NA[d]	NA[b]	NA[b]
54.8	2727	NA[d]	0.1867	NA[d]	NA[d]	0.1264	1833
54.9	2946	NA[d]	0.1594	NA[d]	NA[d]	NA[c]	NA[c]
54.9	2989	6984	0.1427	5.25	1.54	0.0471	1626
64.0	2566	NA[d]	0.0810	NA[d]	NA[d]	0.0392	1208
64.5	3000	NA[d]	0.0825	NA[d]	NA[d]	0.0361	1400
65.5	2990	NA[d]	0.1550	NA[d]	NA[d]	0.0442	1303
67.4	2459	NA[d]	0.1003	NA[d]	NA[d]	0.0432	1208
67.8	3007	NA[d]	0.1615	NA[d]	NA[d]	0.0609	1479
68.8	2952	NA[d]	0.1216	NA[d]	NA[d]	NA[c]	NA[c]
70.3	2806	NA[d]	0.0993	NA[d]	NA[d]	0.0485	1385
72.3	3222	NA[d]	0.1560	NA[d]	NA[d]	0.0471	1232

[a]Not detected by extensometer-LDVT.
[b]Experimental issue.
[c]Could not fit 3rd degree polynomial.
[d]Not reached steady-state.

Table 4
Coefficients of polynomial fit for the potential function Φ.

$f(\varphi^*) = a_n \times \varphi^{*n} + a_{n-1} \times \varphi^{*n-1} + ... + a_0$

	J_0 [J/m^2]	$\log \delta_0$ [log(mm)]	J_{00} [J/m^2]	$\log \delta_{00}$ [log(mm)]	J_{ss} [J/m^2]	δ_{ss} [mm]
a_0	1.8316E+02	−5.6162E+00	−2.9628E+00	−5.3569E+00	5.1288E+02	1.8354E+00
a_1	4.3253E+01	2.1029E−01	6.0709E+01	1.1625E−01	1.5581E+02	6.5854E−02
a_2	4.8279E+00	−4.2877E−03	−4.8528E−01	−1.8833E−03		5.1325E−04
a_3	−1.6440E−01	2.8755E−05	−5.1476E−03	9.8360E−06		
a_4	1.7000E−03		4.9861E−05			
a_5	−4.5088E−06					

References

[1] Pagano N, Schoeppner G. Delamination of polymer matrix composites: Problems and assessment. Compr Compos Mater 2000;433–528.

[2] Turon A, Camanho PP, Costa J, Dávila CG. A damage model for the simulation of delamination in advanced composites under variable-mode loading. Mech Mater 2006;38(11):1072–89.

[3] Camanho P, Davila C. Mixed-mode decohesion finite elements in for the simulation composite of delamination materials. NASA 2002;TM-2002-21:1–37.

[4] Freed Y, Banks-Sills L. A new cohesive zone model for mixed mode interface fracture in bimaterials. Eng Fract Mech 2008;75(15):4583–93.

[5] Liu PF, Islam MM. A nonlinear cohesive model for mixed-mode delamination of composite laminates. Compos Struct 2013;106:47–56.

[6] Li S, Thouless MD, Waas AM, Schroeder JA, Zavattieri PD. Mixed-mode cohesive-zone models for fracture of an adhesively bonded polymer-matrix composite. Eng Fract Mech 2006;73(1):64–78.

[7] Hui CY, Ruina A, Long R, Jagota A. Cohesive zone models and fracture. J Adhesion 2011;87(1):1–52.

[8] Turon A, Costa J, Camanho PP, Dávila CG. Simulation of delamination in composites under high-cycle fatigue. Composites A 2007;38(11):2270–82.

[9] Carreras L, Turon A, Bak BL, Lindgaard E, Renart J, Martin de la Escalera F, et al. A simulation method for fatigue-driven delamination in layered structures involving non-negligible fracture process zones and arbitrarily shaped crack fronts. Composites A 2019;122:107–19.

[10] Robinson P, Galvanetto U, Tumino D, Bellucci G, Violeau D. Numerical simulation of fatigue-driven delamination using interface elements. Internat J Numer Methods Engrg 2005;63(13):1824–48.
[11] Pirondi A, Moroni F. A progressive damage model for the prediction of fatigue crack growth in bonded joints. J Adhesion 2010;86(5–6):501–21.
[12] Pirondi A, Giuliese G, Moroni F. Development of a cohesive zone model for three-dimensional simulation of joint de-bonding/delamination under mixed-mode I/II fatigue loading. Int J Struct Integr 2014;5(3):171–86.
[13] Peng L, Xu J. Fatigue delamination growth of composite laminates with fiber bridging: Theory and simulation. In: 13th International conference on fracture 2013, ICF 2013. Vol. 2. 2013, p. 980–9.
[14] Xu XP, Needleman A. Void nucleation by inclusion debonding in a crystal matrix. Model Simul Mater Sci Fmg 1993;1:111–32.
[15] Ortiz M, Pandolfi A. Finite-deformation irreversible cohesive elements for three-dimensional crack-propagation analysis. Internat J Numer Methods Engrg 1999;44(9):1267–82.
[16] Alfano G. On the influence of the shape of the interface law on the application of cohesive-zone models. Compos Sci Technol 2006;66(6):723–30.
[17] Gu P. Notch sensitivity of fiber-reinforced ceramics. Int J Fract 1993;70(3):253–66.
[18] Sørensen BF. Microscale testing and modelling for damage tolerant composite materials and structures. IOP Conf Ser Mater Sci Eng 2020;942. http://dx.doi.org/10.1088/1757-899X/942/1/012004.
[19] Sørensen BF, Kirkegaard P. Determination of mixed mode cohesive laws. Eng Fract Mech 2006;73(17):2642–61.
[20] Sanchez S, Fern L. Influence of the cohesive law shape on the composite adhesively bonded patch repair behaviour. Composites B 2016;91:414–21.
[21] Chai H. The characterization of Mode I delamination failure in non-woven, multidirectional laminates. Composites 1984;15(4):277–90.
[22] Martin R, Murri G. Characterization of Mode I and Mode II delamination growth and thresholds in AS4/PEEK composites. Compos Mater Test Des 1990;9:251–70.
[23] Fernandes RM, Chousal JA, De Moura MF, Xavier J. Determination of cohesive laws of composite bonded joints under mode II loading. Composites B 2013;52:269–74.
[24] Al-Khudairi O, Hadavinia H, Waggott A, Lewis E, Little C. Characterising mode I/mode II fatigue delamination growth in unidirectional fibre reinforced polymer laminates. Mater Des 2015;66(PA):93–102.
[25] Ramkumar R, Whitcomb J. Characterization of mode I and mixed-mode delamination growth in T300/5208 graphite/ epoxy. 1985, p. 315–35.
[26] Dadej K, Surowska B. Analysis of cohesive zone model parameters on response of glass-epoxy composite in mode II interlaminar fracture toughness test. Compos Theory Pract 2016;16(3):180–8.
[27] Suo Z, Bao G, Fan B. Delamination R-curve phenomena due to damage. J Mech Phys Solids 1992;40(1):1–16.
[28] Sørensen BF, Jørgensen K, Jacobsen TK, Østergaard RC. DCB-specimen loaded with uneven bending moments. Int J Fract 2006;141(1–2):163–76.
[29] Sørensen BF, Jacobsen TK. Characterizing delamination of fibre composites by mixed mode cohesive laws. Compos Sci Technol 2009;69(3–4):445–56.
[30] Erives R, Sørensen BF, Goutianos S. A coupled mix-mode cohesive law based on a cylindrical potential function. Eng Fract Mech 2022;108632.
[31] Needleman A. A continuum model for void nucleation by inclusion debonding. J Appl Mech 1987;54(3):525–31.
[32] Tvergaard V, Hutchinson JW. The influence of plasticity on mixed mode interface toughness. J Mech Phys Solids 1993;41(6):1119–35.
[33] Stigh U, Svensson D. On cohesive laws for delamination of composites. In: European conference on composite materials. 14th. (June):2010, p. 1–10.
[34] Antoniou A, Mikkelsen LP, Goutianos S, Bagemiel O, Gebauer I, Flindt R, et al. Influence of the glass non-crimp fabric intrinsic undulation on the stiffness of the composite ply: A micromechanical approach. IOP Conf Ser Mater Sci Eng 2020;942(1):1–13. http://dx.doi.org/10.1088/1757-899X/942/1/012017.
[35] Suo Z, Bao G, Fan B, Wang TC. Orthotropy rescaling and implications for fracture in composites. Int J Solids Struct 1991;28(2):235–48.
[36] Wang J. An intuitive tutorial to Gaussian processes regression. 2020, URL arXiv:2009.10862.
[37] Sørensen BF, Goutianos S. Mixed Mode cohesive law with interface dilatation. Mech Mater 2014;70:76–93.
[38] Carol I, Prat P, López C. Normal shear cracking model. J Eng Mech 1996;123(8):765–73.
[39] Purslow D. Matrix fractography of fibre-reinforced epoxy composites. Composites 1986;17:289–303.
[40] Grytten F, Sørensen BF, Goutianos S, Joki RK, Jørgensen JK. A micromechanical model of fiber bridging including effects of large deflections of the bridging fibers. Compos Struct 2021;258. http://dx.doi.org/10.1016/j.compstruct.2020.113405.
[41] Sørensen BF, Gamstedt EK, Østergaard RC, Goutianos S. Micromechanical model of cross-over fibre bridging - Prediction of mixed mode bridging laws. Mech Mater 2008;40(4–5):220–34.
[42] Bao G, Ho S, Suo Z, Fan B. The role of material orthotropy in fracture specimens for composites. Int J Solid Struct 1992;29(9):1105–16.
[43] Quaresimin M, Carraro PA, Meneghetti G, Ricotta M. Mixed-mode fatigue of bonded joints in composites: Experiments and modelling. In: Structural integrity and durability of advanced composites: innovative modelling methods and intelligent design. Elsevier; 2015, p. 271–92.
[44] Kenane M, Benzeggagh ML. Mixed-mode delamination fracture toughness of unidirectional glass/epoxy composites under fatigue loading. Compos Sci Technol 1997;57(5):597–605.
[45] Jumel J, Budzik MK, Shanahan ME. Beam on elastic foundation with anticlastic curvature: Application to analysis of mode I fracture tests. Eng Fract Mech 2011;78(18):3253–69.
[46] Joki RK, Grytten F, Hayman B, Sørensen BF. Determination of a cohesive law for delamination modelling - Accounting for variation in crack opening and stress state across the test specimen width. Compos Sci Technol 2016;128:49–57.